

Heat transfer in a molten salt filled enclosure absorbing concentrated solar radiation

Citation for published version:

Amber, I & O'Donovan, T 2017, 'Heat transfer in a molten salt filled enclosure absorbing concentrated solar radiation', *International Journal of Heat and Mass Transfer*, vol. 113, pp. 444-455.
<https://doi.org/10.1016/j.ijheatmasstransfer.2017.04.028>

Digital Object Identifier (DOI):

[10.1016/j.ijheatmasstransfer.2017.04.028](https://doi.org/10.1016/j.ijheatmasstransfer.2017.04.028)

Link:

[Link to publication record in Heriot-Watt Research Portal](#)

Document Version:

Peer reviewed version

Published In:

International Journal of Heat and Mass Transfer

Publisher Rights Statement:

© 2017 Elsevier B.V.

General rights

Copyright for the publications made accessible via Heriot-Watt Research Portal is retained by the author(s) and / or other copyright owners and it is a condition of accessing these publications that users recognise and abide by the legal requirements associated with these rights.

Take down policy

Heriot-Watt University has made every reasonable effort to ensure that the content in Heriot-Watt Research Portal complies with UK legislation. If you believe that the public display of this file breaches copyright please contact open.access@hw.ac.uk providing details, and we will remove access to the work immediately and investigate your claim.

Heat transfer in a molten salt filled enclosure absorbing concentrated solar radiation

I.Amber and T.S.O'Donovan

*Institute of Mechanical Process and Energy Engineering
Heriot-Watt University, Edinburgh,*

EH14 4AS, United Kingdom

Corresponding author: I.Amber, Email: amberity@yahoo.com

Abstract

Numerical simulations of the natural convection driven by the direct absorption of concentrated solar radiation by a high temperature molten salt filled enclosures for height to diameter ratios (H/D) of 0.5, 1 and 2 and Rayleigh numbers 10^7 - 10^{11} is presented. The domain of interest consists of a fluid cavity bounded by rigid adiabatic vertical walls, a heat-conducting bottom wall of finite thickness and an open adiabatic top surface, directly irradiated by a non- uniform concentrated solar flux. The salt volume is first heated non-uniformly by direct absorption of solar radiation and subsequently from the lower absorber plate which is heated by the absorption of the radiation transmitted through the salt.

A Finite Element Method is used to solve the time dependent two dimensional Navier Stokes equations that includes a depth dependent volumetric heat source and temperature dependent thermophysical of molten salts.

Numerical results presented in terms of isotherms and streamlines show a nonlinear temperature profile consisting of distinct layers where thermocapilarity and buoyancy effects are evident. Fluid flow development in the lower layer is found to vary significantly with time and exhibits an initial stage, transitional stage and quasi-steady stages. The magnitude of the natural convection and the duration of each stage is found to decrease as the aspect ratio increases from 0.5 to 2. Calculation of the average heat transfer reveals that the Nusselt Rayleigh number relationship is not uniformly linear and the average heat transfer over the lower boundary surface increased with increasing Ra .

Keywords: Natural convection, Numerical simulation, Molten salt

1. Introduction

Natural convection plays an important role in design, performance and operating costs in many engineering systems and physical applications. In applications such as buildings, power generation, thermal storage, environmental sciences and electronics cooling, natural convection has been found to strongly influence the operating temperatures and temperature fields [1, 2]. natural convection induced by absorption of solar radiation occurring shallow regions of oceans and lakes [3, 4] has been found to have significant influence on the fluid temperature distribution, biological activity and water quality due to the mixing of pollutants and sediments.

In the present study numerical simulations are considered for the natural convection in an enclosure containing molten salt ($\text{KNO}_3\text{-NaNO}_3$) subject solar radiative heating. The principal driving force for the circulation of the fluid comes from the heat exchange from the wall of finite thickness located at the lower boundary.

Natural convection induced by absorption of solar radiation occurring shallow regions of oceans and lakes [3, 4] has been found to have significant influence on the fluid temperature distribution, biological activity and water quality due to the mixing of pollutants and sediments.

The present study is motivated by the interest to understand heat and fluid flow interactions and their dependences on defined control parameter within a novel small scale solar thermal store. The thermal store accomodates a heat conducting absorber plate of finite thicknes at the lower boundary which promotes isothermalisation required to maximise the storage capacity without damaging the storage medium, which can typically sustain temperatures up to 600°C [5, 6]. $\text{KNO}_3\text{-NaNO}_3$ salt (60-40 wt%, m.p. 222°C) has been used up to 565°C in solar thermal energy collection and storage applications, where its thermal stability has been successfully demonstrated without significant degradation [7–10].

Investigation of the interaction between heat transfer and fluid flow in convective thermal transport in many physical systems has been of primary interests since the classical works of Rayleigh and Bernard [11, 12]. Cavities with differentially heated isothermal or iso-flux end walls have formed idealised models for conducting the fundamental studies for understanding these interactions [11, 12]. The differentially heated cavity problem has been ex-

36 tensively studied experimentally and numerically in various contexts (aspect
 37 ratios, geometries, orientation, fluids and control parameters) and several
 38 boundary conditions. A large body of literature exists for natural convection
 39 in differentially heated cavities; three main thermal boundary conditions ex-
 40 ists based on heating phase angles, ϕ [11–13]: (i) Heating from below ($0^\circ <$
 41 $\phi < 90^\circ$), typical Rayleigh Bernard flows (ii) Lateral heating from the side
 42 ($\phi = 90^\circ$) problem and (iii) heating from above ($90^\circ < \phi < 180^\circ$). In these
 43 problems steady state solutions are obtained for idealised isothermal or flux
 44 boundaries conditions by time stepping from a prescribed initial state.
 45 Unlike in the differentially heated cavity problem, for radiation induced nat-
 46 ural convection problems, it is of fundamental significance to understand the
 47 heat and flow behaviour in an enclosure under time dependent heating con-
 48 ditions.
 49 Literature relating to the fluid mechanics and heat transfer interaction in en-
 50 closures, where the primary driving force for the natural convective motion,
 51 is the volumetric absorption of thermal energy is very limited particularly in
 52 high temperature fluids. Webb and Viskanta [14, 15] investigated the natu-
 53 ral convection in rectangular domains heated by radiative flux at a vertical
 54 surface. In the studied domain the primary driving force for the natural con-
 55 vective motion is the volumetric absorption of thermal energy. For two aspect
 56 ratios, thin hydrodynamic boundary layers, a stagnant and stratified central
 57 core and convective flow regimes were revealed. The thin thermal boundary
 58 observed at the vertical walls is associated with a low heat transfer near the
 59 base and high heat transfer at the top of the enclosure. The maximum fluid
 60 temperature in the cavity increased with increasing aspect ratio. The flow
 61 structure revealed a loss of centrosymmetry (eddy centre) characteristic of
 62 natural convection flows in cavities with differentially heated walls due to the
 63 direct heating of the core of the flow by solar radiation within the fluid.
 64 Li and Durbetaki [16] carried out numerical investigations on the radiation
 65 induced transient natural convection boundary layer. In the study a verti-
 66 cal surface of a non-reactive semi-infinite solid was suddenly subjected to a
 67 radiative heat flux source. The time required for the surface temperature to
 68 attain a specified value and drive natural convection was inversely propor-
 69 tional to the square of the radiative heat flux. Onyegebu [17] numerically
 70 demonstrated that natural convection in a rectangular domain subjected to
 71 isotropic radiation at the top surface is developed at low fluid depths and
 72 albedo, while large fluid depths and low surface boundary emissivity sup-
 73 pressed natural convection. Verevchkin and Startsev [18] in a rectangular

74 domain numerically studied thermal convection in a horizontal water layer
 75 cooled from the top and absorbing incident solar radiation. The study iden-
 76 tified three different heat transfer regimes: intermittent convection, steady
 77 state convection and free convection where flow transition were found to oc-
 78 cur at different values for ratios of the downward solar radiation flux at a
 79 depth to heat flux through the interface [18]. Numerical [19–22], experimen-
 80 tal [23, 24] and scaling [25–27] investigations of the unsteady natural con-
 81 vection induced by the absorption of radiation in triangular enclosures have
 82 been reported. These have relevance to the daytime natural convection in a
 83 side arm and in littoral regions in large water bodies. These investigations
 84 report distinct driving mechanisms and flow regimes described as: early flow
 85 transition characterised by the thermal boundary layer development, a tran-
 86 sitional stage marked by the existence of irregular occurring rising plumes
 87 and a quasi-steady state stage.
 88 Recently, Hattori et al. [28, 29] and Harfash [30] performed three dimensional
 89 numerical simulations of convection induced by the absorption of radiation.
 90 In the former, the authors applied a Direct Numerical Simulations (DNS)
 91 technique to simulate direct absorption of radiation in a parallelopiped rele-
 92 vant to deep water bodies subjected to a top solar radiative heating, where
 93 the authors state that investigations are scarce. Results revealed a non-linear
 94 temperature profiles where two distinct layers: an upper stratification region,
 95 due to internal heating, provided by the direct absorption of radiation and
 96 a potentially unstable boundary layer due to the absorption and re-emission
 97 of the residual radiation by the bottom surface are found. The influence of
 98 a non-linear temperature stratification on maximum height thermal plumes
 99 and the mixing driven by rising thermal plumes. Theoretical calculations
 100 to determined the lower mixed layer thickness was presented. Harfash [30]
 101 conducted three dimensional numerical simulations of convection induced
 102 by absorption of radiation based on linear and non linear analysis. The
 103 study reports the linear theory does not predict anything about instability
 104 and only provides boundaries for instability because of the presence of non-
 105 linear terms. However the non-linear stability theory was demonstrated to
 106 overcome the limitations of the linear stability theory and as such is highly
 107 desirable, for full assessment of any subcritical regions.
 108 This paper presents two dimensional numerical simulations for the transient
 109 natural convection in a fixed volume of binary molten $\text{KNO}_3\text{-NaNO}_3$ absorb-
 110 ing concentrated solar radiation in enclosures of height to diameter ratios
 111 (H/D) of 0.5, 1 and for Rayleigh numbers $10^7 - 10^{11}$. The present model

112 accounts for the depth dependent absorption of solar radiation by assum-
 113 ing, the attenuation coefficient is characterised by a single bulk attenuation
 114 coefficient, which is a common practice found in many literatures.

115 2. Geometry and numerical formulation

116 Figure 1, shows a two dimensional schematic of the physical model for
 117 an aspect ratio ($H/D=1$). The enclosure contains molten $\text{KNO}_3\text{-NaNO}_3$
 118 confined between rigid, adiabatic vertical walls and a rigid lower boundary
 119 wall of finite thickness in contact with the molten salt. The top surface is
 120 stress free, open and adiabatic. The sole purpose of the plate located at the
 121 lower boundary is to absorb all radiation transmitted to the lower surface,
 122 subsequently driving a natural convection to heat and mix the molten salt.

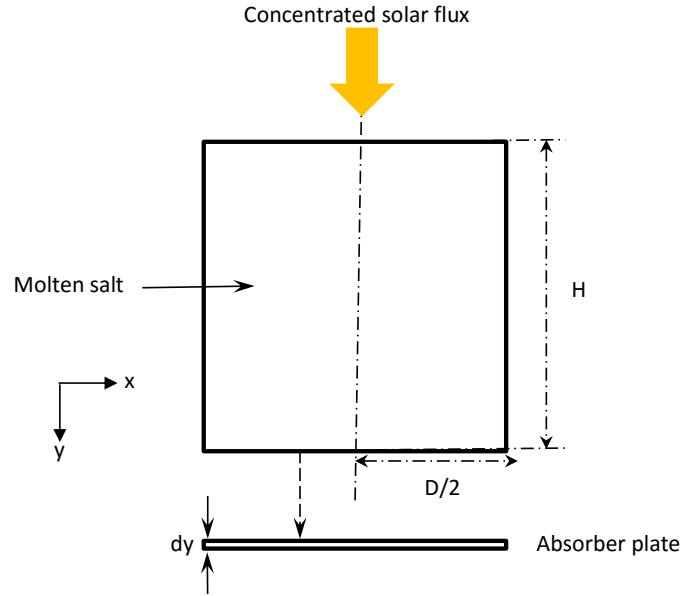


Figure 1: Physical model

123 $\text{KNO}_3\text{-NaNO}_3$ (60%-40% wt) [31] commonly used in sensible heat is as-
 124 sumed to be initially in a liquid and quiescent state and at a temperature,
 125 $T_0=250^\circ\text{C}$, above its crystallisation temperature. The molten salt is assumed
 126 to remain in a molten state for this study.

127 At the time $t=0$, a non-uniform concentrated flux at (700X) is initiated at
 128 the top surface and thereafter maintained.
 129 The solar radiation intensity penetrating downward into the fluid depth ab-
 130 sorbed directly in a non uniform manner is described mathematically by
 131 equation (1)

$$I = CAI_0 e^{(\alpha y)} \quad (1)$$

132 where I is the intensity transmitted through a layer of material of thickness y ,
 133 I_0 is the radiation intensity at the surface y_0 , and α is the solar weighted ab-
 134 sorption coefficient and y represents the vertical coordinate. The volumetric
 135 rate of heat generated can be estimated by:

$$S = \frac{dI}{dy} \quad (2)$$

136 In the present study the non absorbed solar radiation reaching the bottom
 137 surface is assumed to be fully absorbed by a black conducting wall of finite
 138 thickness located at the bottom boundary. The heat exchange at the lower
 139 boundary provides the principal driving force for the fluid circulation.

140 3. Governing Equations

141 It is assumed in the present analysis that the molten KNO_3 - $NaNO_3$ is
 142 Newtonian with temperature dependent properties. Flow is assumed to be
 143 two-dimensional and the fluid top surface is assumed to be optically smooth
 144 and intercepts non uniform concentrated solar flux defined as a Gaussian
 145 profile.

146 The generated temperature and flow fields within the enclosure are governed
 147 by the continuity, momentum and energy transport equations with a source
 148 term as given below equations (3) to (5):

$$\nabla \cdot \vec{V} = 0 \quad (3)$$

$$\rho \frac{\partial(\vec{V})}{\partial t} + \rho(\vec{V} \cdot \nabla) \cdot \vec{V} = -\nabla p + \mu \nabla^2 \vec{V} + \rho g \quad (4)$$

$$\rho C_p \left(\frac{\partial T}{\partial t} + \nabla \cdot \vec{V} T \right) = \nabla \cdot (k \cdot \nabla T) + S \quad (5)$$

149 where \vec{V} is the velocity vector consisting of the velocity components u
 150 and v. T is the spatial temperature in the domain; P is the pressure; S is the
 151 source term representing the rate of absorption of solar radiation given in
 152 a simple form in equation (6) determined by solving the Radiative Transfer
 153 Equation (RTE) subject to the appropriate radiative boundary conditions
 154 and neglecting wavelength dependency, scattering and directional cosines.
 155 Thermo physical properties of molten salt $\text{KNO}_3\text{-NaNO}_3$ (40-60%wt) are
 156 taken for temperature dependent properties which is given in Table 1.

$$S = [1 - \rho_a]\alpha I(e^{\alpha y} + \kappa e^{\alpha L}) \quad (6)$$

157 The first terms on the RHS of equation (6) represent the contributions
 158 of the direct absorption of radiation within the fluid body while the second
 159 term denotes the contribution to the heated absorber plate at the bottom.
 160 Using the following scales: $H \sim \alpha$ (length scale); $t \sim \kappa \alpha^2$ (time scale); T
 161 $\sim g \beta I_0 / C_p \kappa \alpha^2$ (temperature scale); $\vec{V} = (u, v)$, $\sim \kappa \alpha$ (velocity scale),
 162 equation (3) to (5) are non dimensionalised as:

$$\rho \frac{\partial(\vec{V})}{\partial t} + \rho(\vec{V} \cdot \nabla) \vec{V} = -RaPr \nabla p + RaPr \nabla^2 \vec{V} + PrRaT \quad (7)$$

$$\rho C_p \left(\frac{\partial T}{\partial t} + \nabla \cdot \vec{V} T \right) = \nabla \cdot (k \cdot \nabla T) + S \quad (8)$$

163 The controlling parameters describing the flow in an enclosure are given
 164 by the Rayleigh number defined in terms of flux Rayleigh number is given as
 165 shown by equation (9).

$$Ra = \frac{\rho^2 C_p g \beta q H^4}{\mu k^2} \quad (9)$$

166 where g, ρ , μ , k, and β are the gravity, density, viscosity thermal diffusivity
 167 and volumetric expansion constant respectively.

168 The Prandtl number (equation 10) is a fluid property:

$$Pr = \frac{\mu C_p}{k} \quad (10)$$

169 The aspect ratio is defined as shown in equation (11)

$$A = \frac{H}{D} \quad (11)$$

170 where H and D are the height and width. The volume remains constant for
171 all aspect ratios.
172 The dimensionless heat transfer is defined in equation (12)

$$Nu = \frac{qD}{k\Delta T} \quad (12)$$

173 From the transient analysis, the initial conditions are set as follows:

- 174 1. $u, v(t=0)=0$.
- 175 2. $T(t=0)=250\text{K}$ melting point temperature of salt $t \leq 0$.

176 The Boundary conditions are summarised as:

- 177 1. Vertical wall is rigid adiabatic, and impermeable. No slip occurs at the
178 side walls. The velocity components and normal temperature gradients being
179 zero, ($u=v=dT/dn=0$).
- 180 2. The top boundary ($y=0$) is a stress free and adiabatic surface.
181 ($du/dx=dv/dy=dT/dy=0$)
- 182 3. The lower boundary is a rigid wall with no slip ($u=v=0$) and of finite
183 thickness and thermal conductivity, where the transmitted flux to this surface
184 is absorbed and heats the lower fluid at temperatures obtained from equations
185 (13). The temperature of the bottom $y=-H$ is given by:

$$T(t) = T_i + \Delta T \quad (13)$$

186 where, $\Delta T \sim \frac{2I}{k} \left(\sqrt{\frac{\alpha t}{\pi}} \right)^{\frac{1}{2}}$ I is the Total Solar Intensity(TSI) and α is a
187 weighted attenuation coefficient.

Table 1: Thermophysical properties of molten $\text{KNO}_3\text{-NaNO}_3$ salt and properties of absorber plate material [34, 35]

Property/units	$\text{KNO}_3\text{-NaNO}_3$	Copper
ρ (kgm^{-3})	2090-0.636T	8960
k (W (mK) $^{-1}$)	$0.443+1.9 \times 10^{-4}T$	400
C_p (J(kgK) $^{-1}$)	1443-0.172T (1396.044+0.172T)	385
μ ($\text{kg}(\text{ms})^{-1}$)	$22.714-0.12T+2.281 \times 10^{-4}T-1.474 \times 10^{-7}T$	

188 3.1. Numerical implementation

189 The derived time dependent system of non-linear partial differential equa-
190 tions (PDEs) were solved using commercially available Finite Element Method

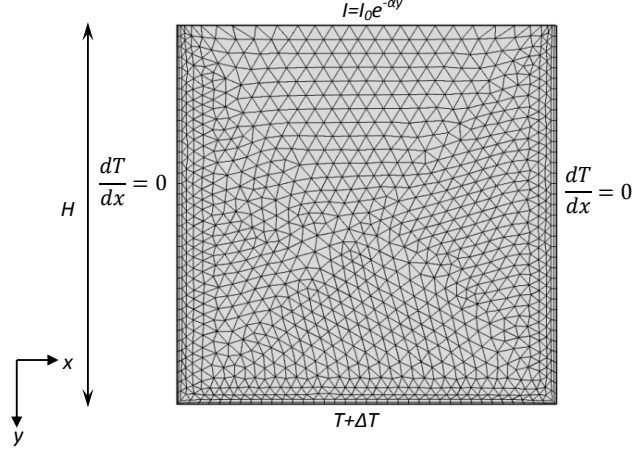


Figure 2: Unstructured computational mesh used in the present study.

191 (FEM) software COMSOL Multiphysics [32]. Second-order and linear el-
 192 ements discretisation were applied for the velocity and the pressure field,
 193 (P_2+P_1). An unstructured mesh consisting of triangular mesh elements is
 194 adopted in the simulation to account for the variability of the formed thermal
 195 plumes and its occurrence at arbitrary locations. Figure 2 shows a schematic
 196 of the unstructured mesh used in the numerical simulations for $H/D=0.5$, 1
 197 and 2.

198

199 In order to ensure mesh-independent solutions, mesh convergence tests
 200 are performed. For a representative simulation for concentration ratio $C =$
 201 $700X$, $I_0 = 1000 \text{ Wm}^2$, and $\alpha = 2 \text{ m}^{-1}$ corresponding to the case $Ra = 10^{11}$,
 202 Figure 3 shows the results of the domain temperature across a mid-vertical
 203 plane for three different mesh resolutions for the cases of $H/D = 0.5$ (Figure
 204 3a), 1 (Figure 3b) and 2 (Figure 3c). Based on the results of the mesh refine-
 205 ment, dimensionless mesh sizes of 0.01, 0.015, and 0.02 was used for $H/D =$
 206 0.5 , 1 and 2. Using these meshes it has been estimated that the relative error
 207 found between the solution at the finest mesh size was found to be below 2%
 208 for temperature solution and was adequate to optimize computational time
 209 without losing numerical accuracy.

210 Effect of time step on the solution were carefully examined for the numerical
 211 results. In Fig 4 the time-step dependence test for results of the time histories

212 for the vertical velocity for time steps: 0.2, 0.5, and 1 s tested is presented.
 213 For example example at $H/D=1$, three stages of the flow development can
 214 be seen. The solutions follow closely to each other, with slight differences
 215 among the solutions for the velocity and predicted flow transition times.
 216 In the present study, as a primary interest is to identify the thermal flow
 217 mechanism and development rather than resolve the details of convective
 218 instability and as a compromise between the computational time and the
 219 accuracy a time step of 1 s is adopted in the numerical calculation. This
 220 time step is found to be is sufficient to resolve and frequency component in
 221 the simulation. Similarly, the three stages of the thermal flow development

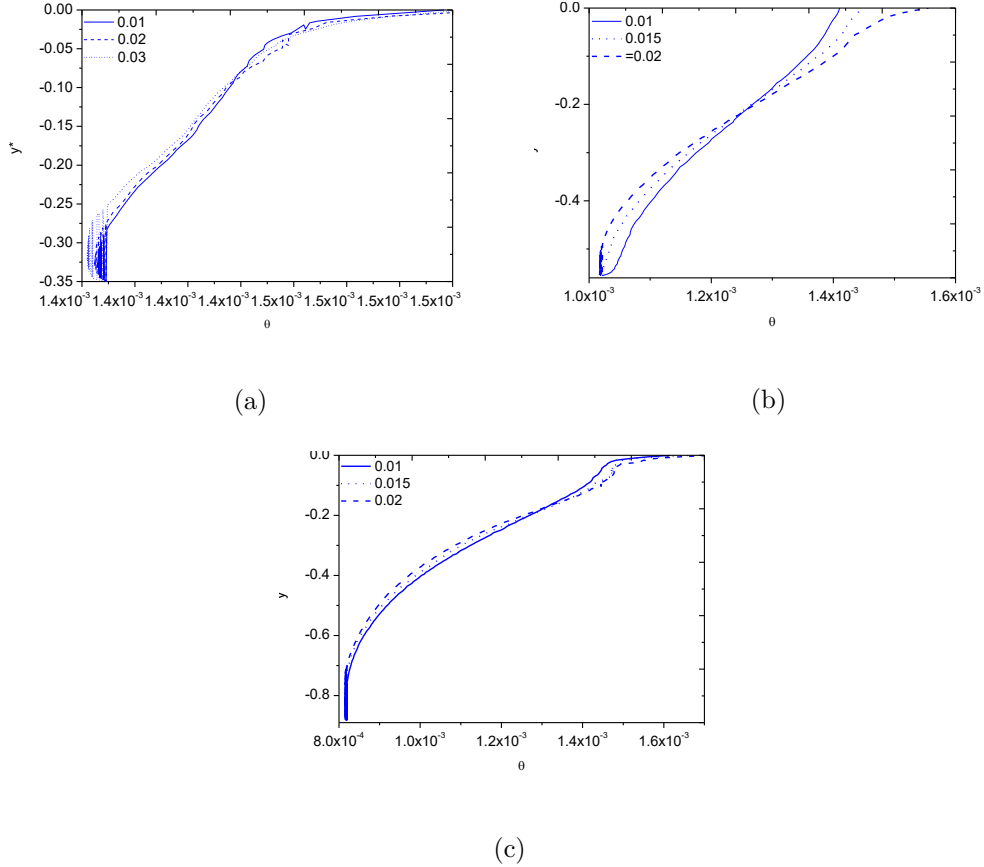


Figure 3: Mesh convergence plot for the temperature taken from the vertical section at $\tau = 4.5 \times 10^{-3}$ (a) $H/D=0.5$ (b) $H/D=1$ (c) $H/D=2$.

222 observed is demonstrated in the solutions obtained at $H/D = 0.5$ and 2. A
 223 convergence criteria of 10^{-5} was imposed for the residuals of the governing
 224 equation.

226 3.2. Validation

227 Due to lack of standard solutions for volumetric absorption of concen-
 228 trated solar radiation in cylindrical enclosures, the model used in the present
 229 study is validated against, the laboratory-scale experiments of Lei and Patter-
 230 son [23] for the natural convection in a horizontal fluid layer of shallow depth
 231 subject to constant and uniform radiation at the water surface. Numerically
 232 predicted temperature distribution along a vertical line is compared against
 233 the experimentally measured values from a water filled flow domain with
 234 measured bulk attenuation coefficient 6.16m^{-1} illuminated by $I_0 = 50\text{W/m}^2$ at
 235 a reference temperature 21.5°C , which gives $\text{Gr} = 2.51 \times 10^6$ and $\text{Pr} = 6.83$.

236
 237 For full description of the laboratory experiment readers are referred to
 238 Lei and Patterson [23]. Fig 5 presents the results for the temperature distri-
 239 bution along the mid-height. The results obtained show a good agreement.
 240 Fig 6 shows a comparison of numerically simulated results and experimen-
 241 tally obtained transient temperature taken within a point in the boundary

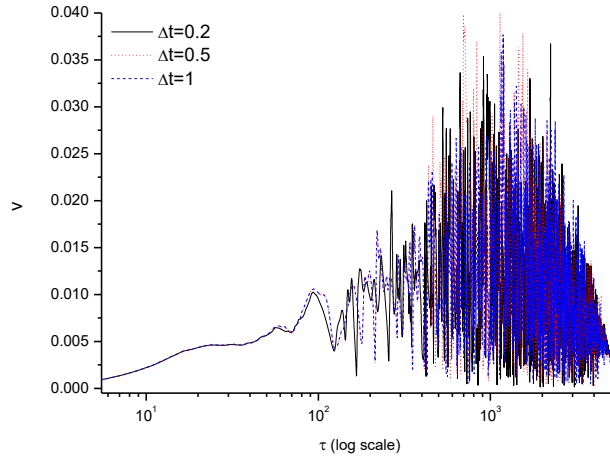


Figure 4: Mesh convergence plot for time history at $H/D=1$ for $\text{Ra} = 10^{11}$

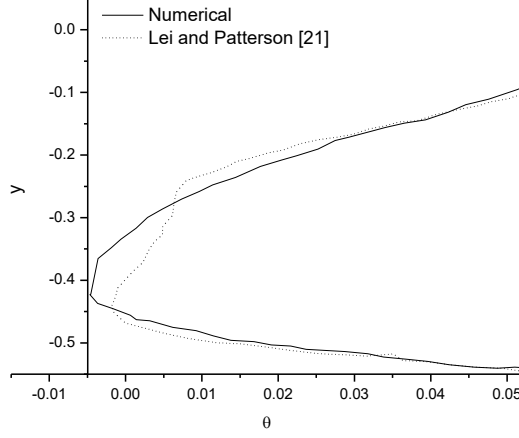


Figure 5: Vertical temperature profile at $x=5.5$ for experiments (dash) [23] and numerical simulation (solid) at $\tau = 0.200$ (5049s).

242 layer. From Fig 6, it can be seen that the comparison is satisfactory between
 243 results. The validation study demonstrates that the model is capable of pre-
 244 dicting natural convection in enclosure subjected to solar radiative heating.
 245

246 4. Results and discussion

247 Fig 4 to Fig 6 present isotherms and velocity streamlines for aspect ratio
 248 0.5, 1 and 2 at dimensionless time steps $\tau = 2.27 \times 10^{-5}$ (30s), $\tau = 1.82 \times$
 249 10^{-3} (2290s), $\tau = 3.81 \times 10^{-3}$ (4650s). The time steps present demonstrate
 250 important thermal and flow features observed during the thermal flow devel-
 251 opment.

252 At $H/D = 0.5$, Fig 7a shows isotherms and corresponding streamlines during
 253 an early heating time, $\tau = 2.27 \times 10^{-5}$ (Fig 7a (i)). At this times step, tem-
 254 perature contours show non uniform heating of the fluid body by the direct
 255 absorption of solar radiation, and a thermal boundary layer formed above
 256 the lower surface. In Fig 7a (ii), the corresponding streamlines indicate flows
 257 of low velocity just below the top surface and no bulk flow circulation within
 258 the fluid body. The convective flow just below the top surface effectively dis-
 259 tributes the heat horizontally; this is achieved in clockwise rotating vortices

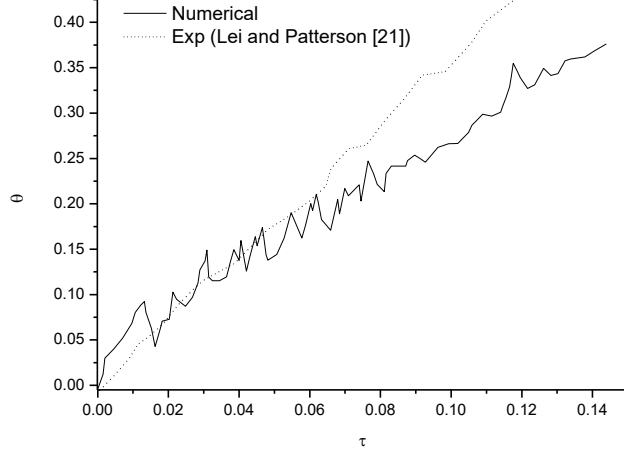


Figure 6: Plot of the time series of temperature in the thermal boundary experiment (dot) and Numerical (solid) layer at $(x,y)=(4.25, 0.016)$.

(Fig 5a (ii)). At a later heating time $\tau = 1.82 \times 10^{-3}$, Fig 7b(i) shows continuous absorption of radiation results in expansion of the isotherms toward the lower surface. The absorbed heat flux from the lower surface continues to contribute to the boundary layer. thermal boundary layer growth continues during this heating stage until the temperate gradient within the boundary layer reaches a critical value that satisfies the stability criterion for convection. Thermal instabilities are then introduced within the thermal boundary marked by the occurrence of thermal plumes. Streamlines (Fig 7b(ii)) show increased fluid circulation, illustrated by the presence of the circulation cells of varying sizes and strength. Fig 7c(i) shows the thermal and flow features at heating time $\tau = 3.81 \times 10^{-3}$. A non linear temperature profile is observed at this time step, where a stratified top layer and a convecting lower stage co-exist. Streamlines (Fig 7c(ii)) also show a fully developed unsteady complex flow.

In Fig 8a (i) and (ii) the temperature contours and streamlines at an early time ($\tau = 2.27 \times 10^{-5}$) is shown for $H/D=1$. The contours indicate the a non-linear absorption of solar radiation with the fluid body and a developing boundary layer at the lower boundary. Similarly, the corresponding streamlines show a convective flow that distributes the heat horizontally just below the top surface achieved in clockwise rotating vortices (Fig 8a (ii)).

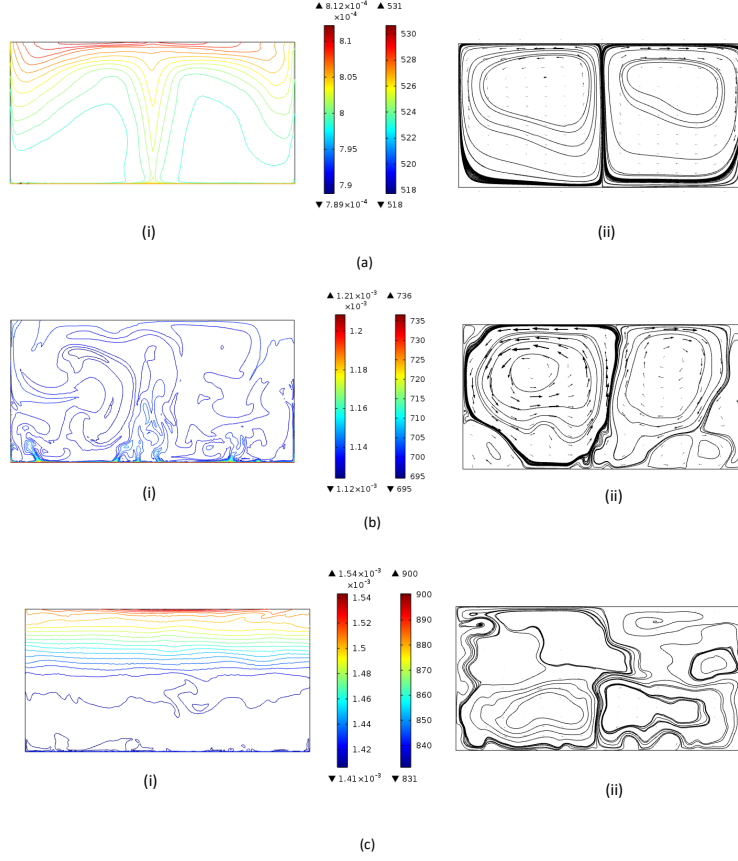


Figure 7: Temperature contours (left) and streamlines (right) for $H/D=0.5$ (a) $\tau = 2.27 \times 10^{-5}$ (b) $\tau = 1.82 \times 10^{-3}$ (c) $\tau = 3.81 \times 10^{-3}$

280 In Fig 8b (i) ($\tau = 1.82 \times 10^{-3}$), a non linear temperature profile is evident
281 where a stable hot surface layer forms above a thermal plume dominated
282 cooler mixing layer. Streamlines in Fig 8b (ii) indicate no flow in the top
283 fluid layer and unsteady flow in the lower fluid layer. Significant differences
284 between the aspect ratios at $H/D= 0.5$ and 1 can be seen from the layout
285 of the thermal and flow features and the time scales at which these transi-

286 tions occur. Fig 8c shows a late heating stage at $\tau = 3.81 \times 10^{-3}$ (Fig 8c(i))
 287 when the enclosure becomes fully stratified, evident from the nearly paral-
 288 lel isotherms. Streamlines (Fig 8c(ii)) at this time indicate no bulk fluid
 289 movement.

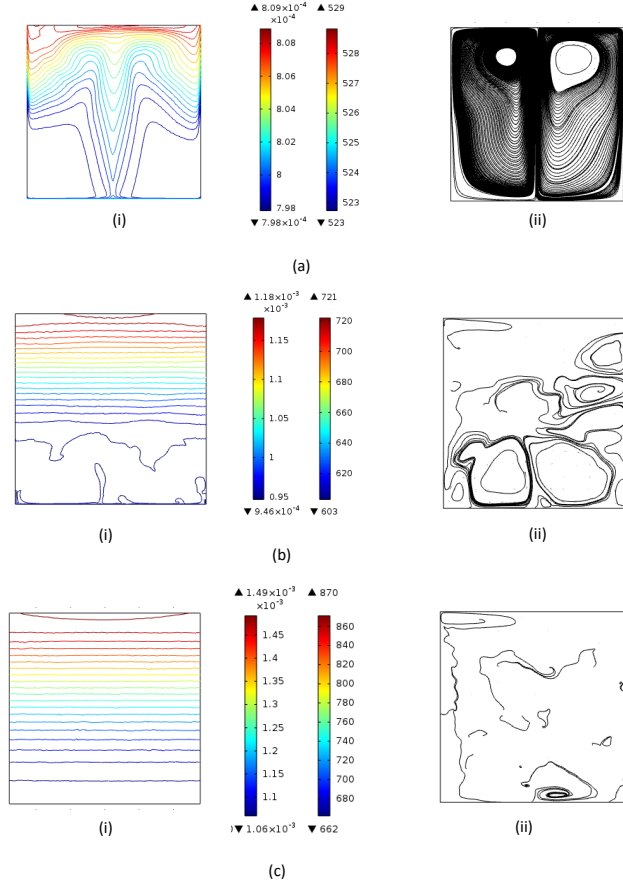


Figure 8: Temperature contours (left) and streamlines (right) for $H/D=1$ (a) $\tau = 2.27 \times 10^{-5}$ (b) $\tau = 1.82 \times 10^{-3}$ (c) $\tau = 3.81 \times 10^{-3}$

290 For $H/D=2$, Fig 9a (i) presents the isotherm at the early heating time
 291 at $\tau = 2.27 \times 10^{-5}$. At later heating times, $\tau = 1.82 \times 10^{-3}$ (Fig 9b(i))
 292 and $\tau = 3.81 \times 10^{-3}$ (Fig 9c (i)); the isotherms have become monotonic and
 293 nearly parallel temperature contours illustrating a primarily a conductive
 294 heat transfer regime. Corresponding streamlines shows no flows in the lower

295 boundary in Fig 9b)(i); weak flows of low intensity in the flow solution at
 296 1.82×10^{-3} (Fig 9b)(ii) in the lower layer and weaker flows of much lower
 297 intensity at 3.81×10^{-3} (Fig 9c (ii)).
 298 From Fig 7 to Fig 9 it can be seen that resulting temperature profiles and
 299 flow patterns that result for a predefined configuration are determined by
 300 a complex interaction between the competing stabilising effect due to the
 301 direct absorption of solar radiation, thermocapillary forces and buoyancy
 302 forces. The top hot surface layer is generally characterised by no bulk fluid
 303 movement [28], however in the current results fluid velocities below the air-
 304 salt interface in the horizontal direction are observed. This is attributed to
 305 the fact that the interface between a liquid and ambient atmosphere is sub-
 306 jected to very high temperature differences and fluid motion is induced. An
 307 identical phenomenon was observed in experiments of Cramer et al.[33] while
 308 heating molten salts in a cylindrical cell, heated by heater located just below
 309 the top surface. As the induced fluid velocities drive flow along the top sur-
 310 face, and down the lateral wall, in the early stages vortices are formed that
 311 are found to be an important mechanism in establishing and maintaining the
 312 top surface layer. In the lower mixing fluid layer confined in a depth below
 313 the stratified the top hot surface layer consists boundary layer development
 314 and thermal plumes. The thermal plumes are observed as important mech-
 315 anisms for the convective mixing within the lower layer.

317 4.1. Flow velocity and heat transfer time histories

318 Figure 10 a-c shows the time history for the vertical flow velocity at a
 319 point $(x, y) = (0, 0.98H)$, within the bottom boundary for $H/D = 0.5, 1$ and
 320 2 . For the three aspects, the plot for the flow velocity in 10 a, b and c
 321 presents the three distinct flow regimes classified as early, transitional and
 322 quasi steady marked by i-iii respectively.
 323 In Fig 10a, $H/D = 0.5$, the early flow (i) occurs for $\tau < 3.79 \times 10^{-5}$ after solar
 324 radiative heating is initiated. This flow regime is marked by the development
 325 of the diffusive growth of a bottom thermal boundary layer. During this stage
 326 the flow velocity smoothly increases from quiescent state to a maximum value
 327 corresponding to the initial peak as can be seen in the log scale plot insert
 328 in Fig 10a. For heating times $3.79 \times 10^{-5} < \tau < 6.73 \times 10^{-3}$, soon after the
 329 initial peak, a sharp drop in the velocity from a maximum value is revealed
 330 where after the velocity fluctuates with time in sharp irregular oscillations
 331 of varying amplitudes. This marks the transitional stage denoted by (ii)

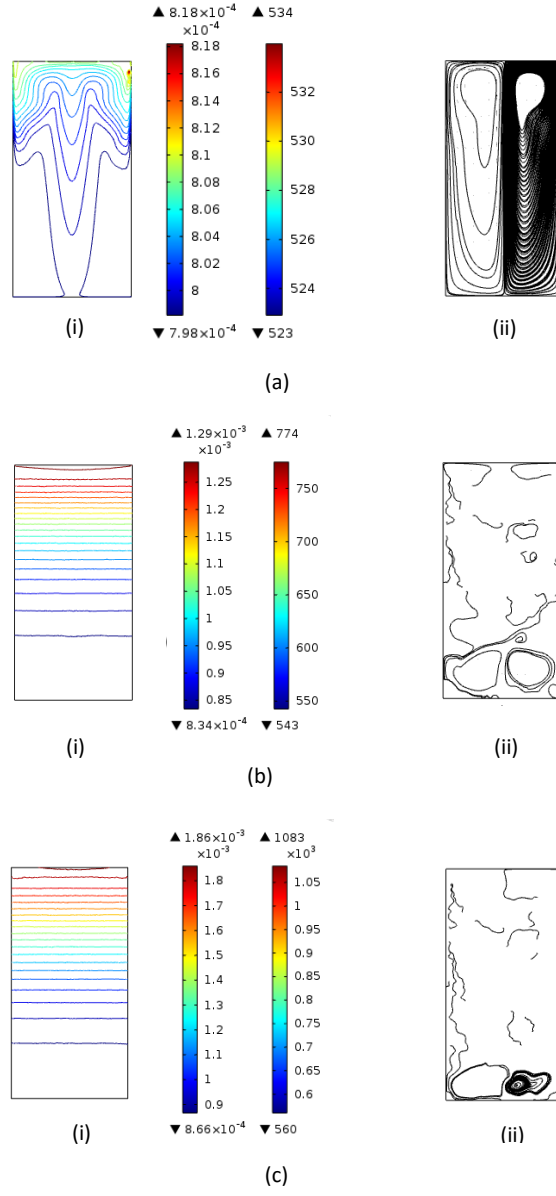


Figure 9: Temperature contours (left) and streamlines (right) for $H/D=2$ (a) $\tau = 2.27 \times 10^{-5}$ (b) $\tau = 1.82 \times 10^{-3}$ (c) $\tau = 3.81 \times 10^{-3}$

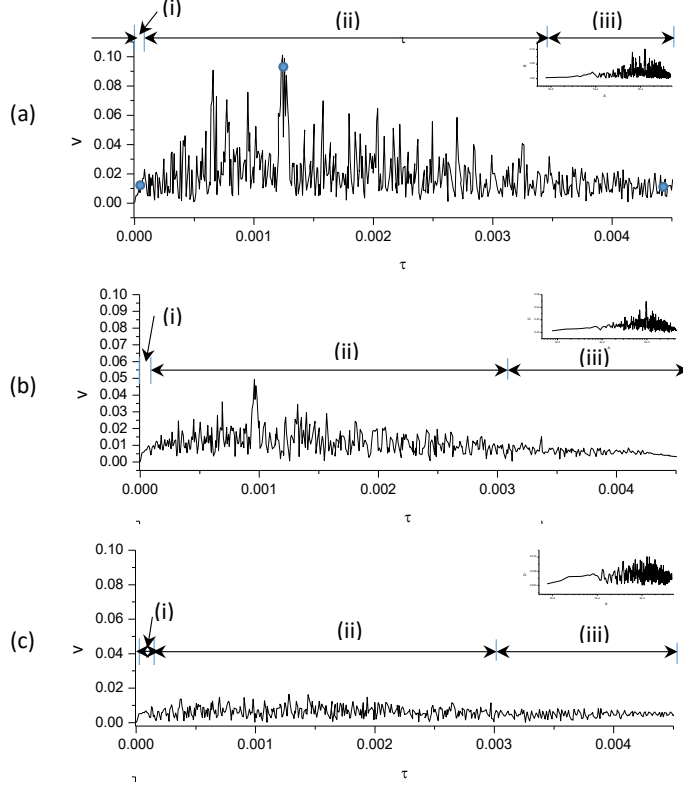


Figure 10: Time series of the flow velocity for $H/D=0.5$, 1 and 2

332 marked by the existence of thermal instability (ii). The velocity fluctuations
 333 and oscillations with time corresponds to the formation and detachment of
 334 rising plumes from the boundary layer. The flow velocity then reaches a
 335 quasi-steady state (iii) for heating times $\tau > 6.73 \times 10^{-5}$. During this stage
 336 the flow velocity decreases in oscillations and amplitudes which tends to ap-
 337 proximately a constant value (Fig 10a). This occurs due to the fluid layer
 338 becomes mostly stratified and the convective flow being suppressed and con-
 339 fined within the boundary layer.
 340 Similarly, for $H/D = 1$ (Fig 10b) and $H/D = 2$ (Fig 10c), an early (i), tran-
 341 sitional (ii), and quasi-steady (iii) flow stages can be easily identified.

342 The main differences between the aspect ratios are the time scale at which
343 these transitions occur, the magnitude, amplitude and oscillation of fluctua-
344 tions. These differences can easily be matched with isotherms and streamlines
345 presented in Fig 7 to Fig 9.
346 The magnitude of the flow velocity and the amplitude of oscillations within
347 the transitional regime decrease with increasing aspect ratio. Time for the
348 occurrence of the first dip that corresponds to change from the initial stage
349 to the transitional stage and thermal plumes initiation is found to shift to
350 higher times with increasing aspect ratio. This is due to an increase in the
351 percentage of the incident radiation absorbed within the salt and reduction in
352 the amount radiation is transmitted to the bottom boundary with increasing
353 aspect ratio. Therefore resulting in lower heating at the bottom boundary at
354 higher aspect ratio. Table 2 presents time scales for identified flow regimes
355 for the respective aspect ratios in Figure 10 a, b and c.

Table 2: Flow regime time scales for H/D=0.5, 1 and 2

	0.5	1	2
i	$\tau < 8.34 \times 10^{-5}$	$\tau < 1.14 \times 10^{-4}$	$\tau < 1.29 \times 10^{-4}$
ii	$8.34 \times 10^{-5} < \tau < 3.12 \times 10^{-3}$	$1.14 \times 10^{-4} < \tau < 2.93 \times 10^{-3}$	$1.29 \times 10^{-4} < \tau < 2.52 \times 10^{-3}$
iii	$\tau > 3.12 \times 10^{-3}$	$\tau > 2.93 \times 10^{-3}$	$\tau > 2.52 \times 10^{-3}$

356 Fig 11 presents the time history for the heat transfer from the lower sur-
357 face for Ra value of 8.9×10^{11} for H/D=0.5, 1 and 2. Three distinct regions
358 can be seen in Fig 11.
359 At H/D=0.5, in the early stage which occur for $\tau < 8.34 \times 10^{-5}$ the heat
360 transfer increases sharply during this stage to a maximum (Fig 11) for all as-
361 pect ratios. As no significant flow exists at this stage, heat transfer from the
362 lower plate is dominated by conduction and establishes a thermal boundary
363 layer in the region just above the lower plate. The heat transfer reaches a
364 local minimum at $\tau < 8.34 \times 10^{-5}$ and then increases into a region of irregular
365 fluctuations before reaching a nearly constant value, where the rate of heat
366 transfer is becomes reduced with reduced fluctuations and amplitude. The
367 presence of the first dip in Fig 11, corresponds approximately to the change
368 from the initial stage to the transitional stage ($\tau < 8.34 \times 10^{-5}$). The high
369 heat transfer rates in the transition stage correspond to the occurrence of
370 thermal plumes. At the quasi-steady state, the heat transfer decreases due
371 to the increase in bulk fluid temperature. Thus, the transient heat trans-
372 fer response is characterised by three regimes: conduction in the early flow

373 regime, convection in the transitional stage and quasi steady. The driving
 374 mechanisms for heat transfer here can easily be matched with the major fluid
 375 developments and features identified from the averaged flow rate in Fig 11.
 376 The transient heat transfer at $H/D=1$ is similar to that at $H/D=0.5$. The
 377 main differences between the two aspect ratios are the time scale at which
 378 heat transfer transitions occur and the magnitude. The heat transfer from
 379 the lower surface is found to decrease by 55% when the aspect ratio changes
 380 from $H/D=0.5$ to $H/D=1$. For $H/D=2$, the sharp spike in the heat trans-
 381 fer at the early stage is observed, where after transcends into a transitional
 382 regime with much reduced amplitudes and then into the quasi steady state.
 383 Heat transfer at this height is found to decrease by 70% and 30% compared
 384 to $H/D=0.5$ and $H/D=1$ respectively. The plots reveal features that are con-
 385 sistent with those presented in Fig 10 and the driving mechanisms for heat
 386 transfer here can easily be matched with the major fluid developments and
 387 features identified from the isotherms and streamlines presented in Fig 7-9.
 388
 389 As a significant consequence of the nonlinear temperature stratification is the

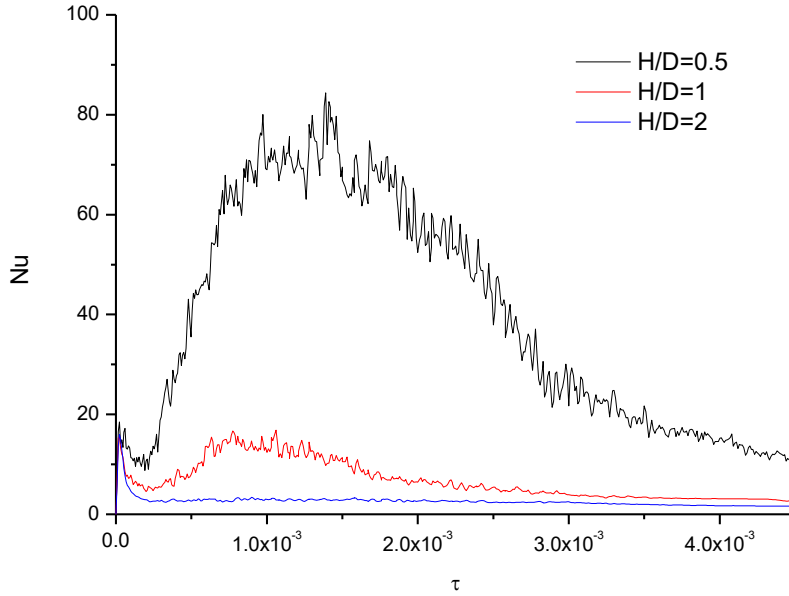


Figure 11: Time series of the heat transfer rate for $H/D=0.5$, 1 and 2

390 limitation of the mixing driven by rising thermal plumes with the penetration
391 length scale of the plumes determining the lower mixed layer thickness. It
392 can be seen that the increase in aspect ratio from 0.5 to 2 and stratification is
393 promoted the plume penetration and mixing depth decrease which coincides
394 with the decrease in heat transfer with increasing aspect ratio.

395 5. Rayleigh number effect on thermal and flow features

396 In this section the effects of variation of Ra on the heat transfer and fluid
397 flow is examined. Fig 12 shows the time averaged temperature contours, av-
398 eraged over $\tau = 1.52 \times 10^{-4}$ to 6.142×10^{-4} in the transitional stage for values:
399 a) $Ra = 10^7$ b) $Ra = 10^8$ c) $Ra = 10^9$ d) $Ra = 10^{10}$ e) $Ra = 10^{11}$ at $H/D = 0.5, 1$ and
400 2. At $H/D = 0.5$, it is seen that the plume penetration height and the inten-
401 sity of plume occurrences increase with increasing values of Ra. The flow in
402 the lower layer exhibits an increasingly complex behaviour with increasing
403 Ra increases. Observations for $H/D = 1$ and 2 reveal that for each aspect
404 ratio increased flows are found to occur with increasing Ra. From these plots
405 it can also be seen that fluid flow corresponding to a particular Ra decreases
406 with increasing aspect ratio.

407 Fig 13 shows time averaged Nusselt number at the lower boundary at differ-
408 ent Ra. It can be seen that heat transfer is dominated by conduction for low
409 Rayleigh numbers ($Ra < 10^7$). Convection starts from $Ra = 10^7$ at $H/D = 0.5$,
410 $Ra = 10^8$ at $H/D = 1$ and $Ra > 10^9$ at $H/D = 2$. The Nusselt number is highest
411 in the shallow domain, $H/D = 0.5$ and lowest at $H/D = 2$. At $Ra = 10^{10}$ the
412 heat transfer is lower by 65% for $H/D = 2$ than that for $H/D = 1$ and it is
413 higher by a factor of 1.38 for than that for at $H/D = 2$.

414 Generally the conduction/transition/convection regimes, as found in cav-
415 ity flows with differentially heated ends emerge as the Rayleigh number in-
416 creases. However, the isotherms and streamline obtained here are different
417 from those obtained in differentially heated cavities as extensively presented
418 in [11–13]. The penetrating radiation in the fluid layer which directly heats
419 the fluid in the interior of the cavity destroys the central symmetry of the
420 system that relates the clockwise flow characteristic of natural convection in
421 cavities with differentially heated side walls. The surface layer stability also
422 increases with increasing Ra as indicated at the respective isotherms and
423 streamlines.

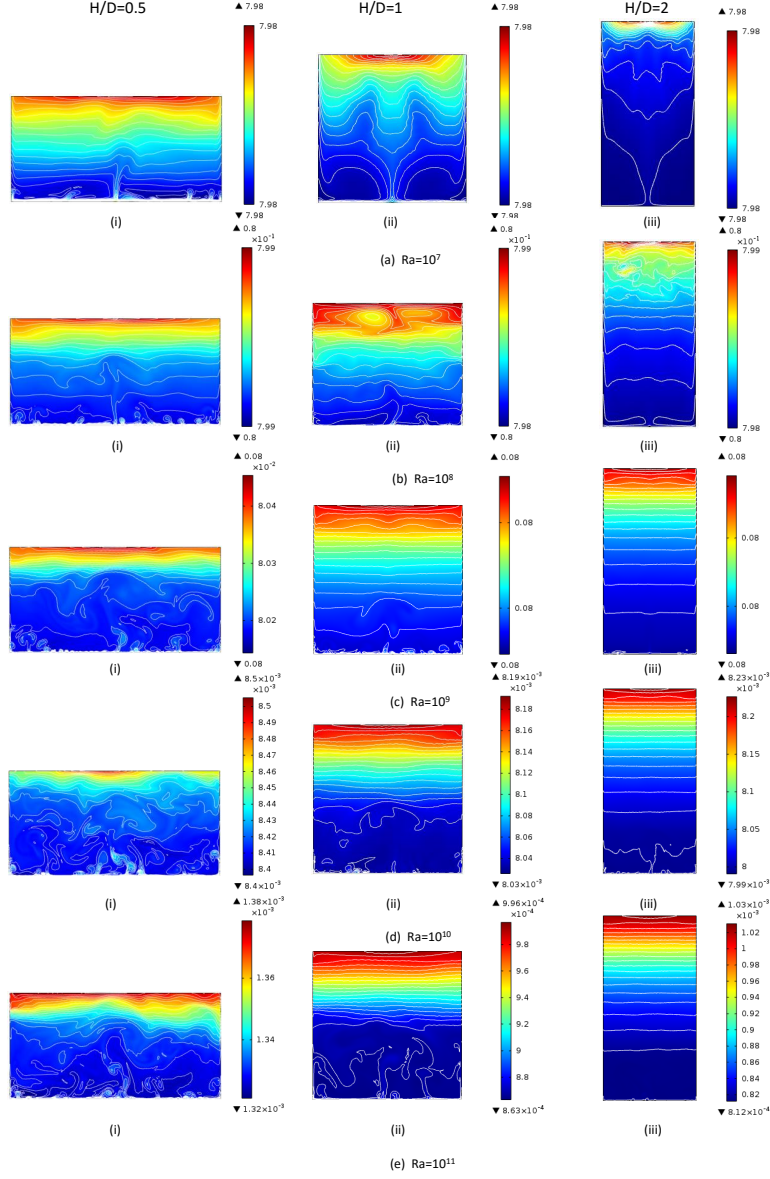


Figure 12: Time averaged temperature contours excluding the quasi steady regime at $H/D=0.5$ for Rayleigh numbers a) $Ra=10^7$ b) $Ra=10^8$ c) $Ra=10^9$ d) $Ra=10^{10}$ e) $Ra=10^{11}$ for $H/D=0.5$ (left column), $H/D=1$ (middle column) and $H/D=2$ (right column)

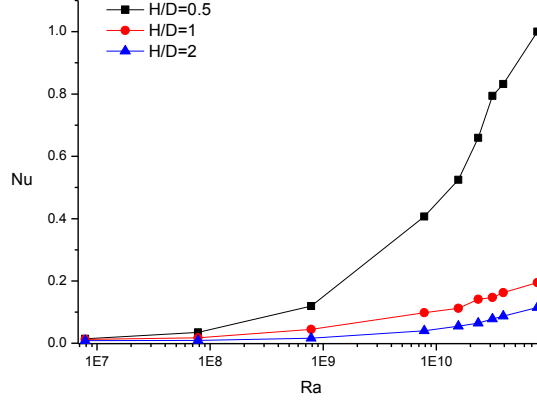


Figure 13: Nusselt number versus the Rayleigh numbers ($10^7 \leq Ra \leq 10^{11}$) at $H/D=0.5$ (black) , $H/D=1$ (red) and $H/D=2$ (blue)

6. Conclusion

Two dimensional numerical models have been developed to simulate the transient heat transfer and fluid flow in molten binary KNO_3 - $NaNO_3$ salt, directly absorbing concentrated solar radiation. The numerical domain consists of molten binary KNO_3 - $NaNO_3$ salt bounded by an open, adiabatic top surface, rigid and adiabatic vertical walls, and a rigid black heat conducting boundary of finite thickness. The developed numerical model accounts for the depth dependent nonlinear volumetric absorption of directly deposited solar radiation based on weighted average values for the solar radiation and the salts attenuation coefficient. The governing equations for the numerical simulations have been carried out using commercial COMSOL Multiphysics software. Numerical simulations were conducted for a charging period of 3 hours used in conjunction with a solar system. Two dimensional numerical results revealed a nonlinear temperature profile consisting of a hot stratified fluid layer lying above a cooler mixing layer. The observed nonlinear temperature was found to occur due to the absorption of radiation within the fluid body being a stabilising force, and the thermal instability at the lower surface being a destabilising force. In the top fluid layer Maragoni convection is observed in the region below the top surface, however no bulk flow of fluid is observed. In this layer heat is transferred primarily by conduction. In the lower fluid layer, where convective heat transfer was observed to dominate,

the observed flow regimes are classified into 3 distinct regimes: (1) an initial stage (conduction regime) (2) a transitional stage (evolution of instabilities and onset of convection) and (3) quasi steady state (convective flow). The average heat transfer is found to decrease with increasing aspect ratio from 0.5 to 2 and increase with Rayleigh number. The average heat transfer calculation also revealed that the Nusselt Rayleigh number relationship is not uniformly linear and the average heat transfer number over the lower boundary surface approximately scales with the aspect ratio. The present study contributes to understanding of the physical processes of solar energy deposition in molten salt necessary in informing rational system design, predict system performance and providing design recommendations necessary for the store to be competitive.

References

- [1] Reymond, O., Murray, D.B. and O'Donovan, T.S., 2008. *Natural convection heat transfer from two horizontal cylinders*. Experimental Thermal and Fluid Science, 32(8),(1702-1709).
- [2] Incropera, F. P. and Lavine, A. S. and Bergman, T. L. and DeWitt, D. P. *Principles of heat and mass transfer*. Wiley, New York, 2013.
- [3] Adams, E.E., Wells., S.A *Field measurements on side arms of lake*. J. Hydraul., Eng. 110 (773793), 1984.
- [4] Monismith, S.G., Imberger, J., Morison, M.L.. *Convective motions in the sidearm of a small reservoir*. Journal Limnol. Oceanogr., (16761702, 1990.
- [5] Slocum, A.H, Codd, D.S, Buongiorno, J., Forsberg, C., McKrell, T., Nave, J.C, Papanicolas, C.N, Ghobeity,A., Noone, C.J, Passerini, S., Rojas, F., Mitsos, A. *Concentrated solar power on demand* Solar Energy, Volume 85, Issue 7, July 2011, Pages 1519-1529, 2011.
- [6] Amber, I., O'Donovan, T.S. *Design and operation of a direct solar absorption sensible heat thermal energy storage system*. Conference Proceedings EURO THERM Seminar No. 98 Concentrating Solar Energy Systems, pp 2013

- 477 [7] Peng, Q., Wei, X., Ding, J., Yang, J., Yang, X., 2008. *High-temperature*
478 *thermal stability of molten salt materials*. International Journal of Energy
479 Research 32, 11641174
- 480 [8] Delameter W. R, Bergan N. E, *Sandia Report* SAND86-8249. (1990)
- 481 [9] Zhou, D., Eames, P *Thermal characterisation of binary sodium/lithium*
482 *nitrate salts for latent heat storage at medium temperatures*. Solar Energy
483 Materials and Solar Cells Volume 157, Pages 10191025 2016.
- 484 [10] Gimenez, P., Fereres S. *Effect of heating rates and composition on the*
485 *thermal decomposition of nitrate based molten salts*. Energy Procedia 69,
486 2015 pp 654 662
- 487 [11] Chandrasekhar, S. *Hydrodynamic and hydromagnetic stability*. Courier
488 Corporation, 2013.
- 489 [12] Drazin, P. G. and Reid, W. H. *Hydrodynamic and hydromagnetic stabil-*
490 *ity*. Cambridge university press, 2004.
- 491 [13] Ostrach, S. *Natural convection in enclosures*. Journal of Heat Transfer,
492 110(4b):1175-1190, 1988.
- 493 [14] Webb, B.W. and Viskanta, R. *Radiation-induced buoyancy-driven flow*
494 *in rectangular enclosures: experiment and analysis*. American Society of
495 Mechanical Engineers, Journal of Heat Transfer, 109(2):427-433, 1988.
- 496 [15] Webb, B.W. and Viskanta, R. *Analysis of radiation-induced natural con-*
497 *vection in rectangular enclosures*. Journal of Thermophysics and Heat
498 Transfer, vol. 1:146-153, 1987
- 499 [16] Li, X. and Durbetaki, P. *The conjugate formulation of a radiation in-*
500 *duced transient natural convection boundary layer*. International journal
501 for numerical methods in engineering, 35(4):853-870, 1992
- 502 [17] Onyegegbu S. *Solar-radiation induced natural-convection in stagnant*
503 *water layers*. Energy Conversion and Management;30:91-100, 1990.
- 504 [18] Verevchkin Y.G., Startsev S.A. *Solar-radiation induced natural-*
505 *convection in stagnant water layers*. Journal of Fluid Mechanics ;421:293-
506 305, 2000.

- 507 [19] Lei,C. and Patterson,J. C. *Unsteady natural convection in a trian-*
508 *gular enclosure induced by absorption of radiation.* Journal of Fluid
509 Mechanics;460(4):181-209, 2002.
- 510 [20] Lei,C. and Patterson,J. C. *Natural convection in a reservoir sidearm*
511 *subject to solar radiation: a two-dimensional simulation.* Numerical Heat
512 Transfer: Part A: Applications;42(1-2):13-32, 2002
- 513 [21] Lei,C. and Patterson,J. C. *A direct three-dimensional simulation of*
514 *radiation-induced natural convection in a shallow wedge.* International
515 Journal of Heat and Mass Transfer;46(7):1183-1197, 2003
- 516 [22] Coates, M. J. and Patterson, J. C. *Numerical simulations of the natural*
517 *convection in a cavity with nonuniform internal sources.* International
518 journal of heat and fluid flow; 15,(3):218–225, 1994
- 519 [23] Lei,C. and Patterson,J. C. *Natural convection in a reservoir sidearm*
520 *subject to solar radiation: experimental observations.* Experiments in
521 Fluids;32(5):590-599, 2002.
- 522 [24] Coates, M. J. and Patterson, J. C. *Unsteady natural convection in*
523 *a cavity with non-uniform absorption of radiation.* Journal of Fluid
524 Mechanics;133-161, 1993
- 525 [25] Mao, Y. and Lei,C. and Patterson,J. C. *Unsteady natural convection in*
526 *a triangular enclosure induced by absorption of radiation—a revisit by im-*
527 *proved scaling analysis.* Journal of Fluid Mechanics;622(5):75-102, 2009.
- 528 [26] Lei,C. and Patterson,J. C. *A direct stability analysis of a radiation-*
529 *induced natural convection boundary layer in a shallow wedge.* Journal of
530 Fluid Mechanics;480:161-184, 2003
- 531 [27] Coates, M. J. and Patterson, J. C. *Characteristics of instability of*
532 *radiation-induced natural convection in shallow littoral waters.* Interna-
533 tional Journal of Thermal Sciences;49(1)170–181, 2010
- 534 [28] Hattori, T. and Patterson, J.C. and Lei, C. *Mixing in internally heated*
535 *natural convection flow and scaling for a quasi-steady boundary layer.*
536 Journal of Fluid Mechanics;763 352-368, 2015

- 537 [29] Hattori, T. and Patterson, J.C. and Lei, C. *Scaling and direct stability*
538 *analyses of natural convection induced by absorption of solar radiation*
539 *in a parallelepiped cavity*. International Journal of Thermal Sciences:88
540 19-32, 2015
- 541 [30] Harfash, A. J. *Three dimensional simulations and stability analysis for*
542 *convection induced by absorption of radiation*. International Journal of
543 Numerical Methods for Heat & Fluid Flow:25(4) 810–824, 2015
- 544 [31] Coastal Chemical Co., LLC. *Hitec Heat Transfer Salt Technical Bulletin*,
545 *Coastal Chemical Co., LLC*.
- 546 [32] Introduction to COMSOL Multiphysics *COMSOL user's guide*
- 547 [33] Cramer, A., Landgraf, S., Beyer, E., Gerbeth, G. *Marangoni convection*
548 *in molten salts* Experiments in Fluids:50(2) 479–490, 2011
- 549 [34] Janz, G. J. *Molten salts handbook* Academic Press, 1967
- 550 [35] Sohal, S. M. and Ebner, A. M. and Sabharwall, P. and Sharpe, P. *En-*
551 *gineering Database of Liquid Salt Thermophysical and Thermochemical*
552 *Properties* Report Idaho National Laboratory. 2010

Nomenclature

A	receiver Area	m^2
C	Concentration ratio	
C_p	Heat capacity	$\text{J}(\text{kgK})^{-1}$
D	Diameter	m
g	Acceleration due to gravity	ms^{-2}
H	Height	m
h	Mesh Element size	m
I	Solar irradiation	Wm^{-2}
k	Thermal conductivity	$\text{W}(\text{mK})^{-1}$
κ	Thermal diffusivity	m^2s^{-1}
Nu	Nusselt number	
P	Pressure	Pa
Pr	Prandtl number	
Q	Volumetric heat generation	Wm^{-3}
\dot{Q}	Volumetric flow rate	m^3s^{-1}
q	Heat flux	Wm^{-2}
Ra	Rayleigh number	
T	Temperature	K
t	Time	s
u	x velocity component	ms^{-1}
v	y velocity component	ms^{-1}
w	z velocity component	ms^{-1}
y^*	Dimensionless height	
α	Absorption coefficient	m^{-1}
τ	Dimensionless time	
μ	Dynamic viscosity	Nsm^{-2}
ν	Kinematic viscosity	m^2s^{-1}
ρ	Density	kgm^{-3}
θ	Dimensionless temperature	